# Intersubband and interminiband spectroscopy of doped and undoped CdS/ZnSe multiple quantum wells and superlattices

M. Göppert, M. Grün, C. Maier, S. Petillon, R. Becker, A. Dinger, A. Storzum, M. Jörger, and C. Klingshirn*
*Institut für Angewandte Physik, Universität Karlsruhe, D-76128 Karlsruhe, Germany*
(Received 26 February 2001; revised manuscript received 10 July 2001; published 8 March 2002)

In cubic CdS/ZnSe type-II heterostructures collective excitations have been studied using infrared spectroscopy. The CdS/ZnSe structures were grown by solid-source molecular-beam epitaxy on semi-insulating GaAs substrates. Highly *n*-type-doped multiple-quantum-well and superlattice samples show strong intersubband and interminiband absorption in the midinfrared. The validity of the polarization selection rule is verified experimentally. The CdS/ZnSe conduction band offset is determined using a combination of interband and intersubband spectroscopy. Measured transition energies agree well to model calculations if many-body effects and band nonparabolicity are included. Intensity-dependent pump and probe measurements on doped and undoped samples reveal a fast increase of the photoinduced absorption signal at low pump intensities. At high pump intensities the absorption signal saturates. This behavior is explained by the existence of a subgroup of long-lived photogenerated electron-hole pairs. An observed redshift of the photoinduced interminiband transitions is explained by filling of the lowest miniband. The effective electron mass of cubic CdS is determined from thick films using infrared reflection spectroscopy.

DOI: 10.1103/PhysRevB.65.115334 PACS number(s): 73.21.−b, 78.30.Fs, 78.66.Hf

## I. INTRODUCTION

Since the first observation of intersubband transitions in quantum wells by means of Raman[1] or infrared spectroscopy,[2] intense investigations of these transitions have been performed. The main emphasis of these investigations has been put on III-V compound[3] and Si/SiGe heterostructures,[4] motivated by infrared detector[5] and laser[6] applications. In II-VI compound heterostructures, intersubband transitions have been observed so far in the small-gap (Cd,Hg)Te system.[7] Only a few wide-gap II-VI heterostructures offer tolerable lattice mismatch, sufficient band offset, and high dopability. The type-II systems CdS/ZnSe and CdSe/ZnTe provide moderate lattice mismatches and large offsets, but only the former allows high doping in both the barrier and well material.

In this paper we report on the first investigation of intersubband transitions in the type-II CdS/ZnSe system. The CdS/ZnSe heterostructures were prepared in our own group. In these structures, electrons are confined in the CdS layers and holes in the ZnSe layers. The conduction band offset has been determined recently to be around 0.8 eV.[8] In order to observe an intersubband or interminiband transition, the lowest subband or miniband has to be populated, either by doping or by photogenerated carriers. High n-type doping levels are attainable in both ZnSe and CdS, with free-electron concentrations up to $1.4\times10^{19}$ $cm^{-3}$ and $8\times10^{19}$ $cm^{-3}$, respectively.[9] Consequently, two-dimensional electron gas densities in excess of $1\times10^{13}$ $cm^{-2}$ were observed in modulation-doped structures.[10]

A second interesting feature of the CdS/ZnSe system relies on the fast relaxation from the higher subbands to the ground state. The rate of this relaxation is governed by the Fröhlich electron-phonon interaction,[11] which is stronger in II-VI materials than in III-V ones. A II-VI-based quantum well infrared detector is therefore potentially faster. The high dopability, the large conduction band offset, and the relatively strong Fröhlich coupling put the CdS/ZnSe system in a position to be an interesting material for fast midinfrared detectors. The present paper studies properties of intersubband and interminiband transitions in CdS/ZnSe multiple quantum wells (MQW's) and superlattices (SL's). The measured transition energies are reproduced by a theory which includes many-body effects and band nonparabolicity. In order to reduce the number of adjustable parameters, the electron band edge mass of cubic CdS has been determined independently from thick films. By varying the ground-state population through photopumping of the interband transition, the two-dimensional electron gas in the MQW's is studied.

## II. EXPERIMENT

The cubic CdS/ZnSe samples were grown on semi-isolating GaAs(001) substrates by solid-source molecular-beam epitaxy.[12] They consist of a 300-nm ZnSe buffer layer followed either by an MQW structure of 20 quantum wells or by a superlattice of 140 periods. The lattice mismatch between CdS and ZnSe is nearly 3% and allows coherent growth only up to about 4.5 nm. The CdS layer thickness was mostly between 2 and 3 nm (6–10 monolayers). Thicknesses were deduced from beam flux pressures as monitored by an ion gauge and referred to as ''nominal thickness.'' The samples were *n*-type doped with different chlorine concentrations, either in the barriers or in the wells. The samples discussed are basically two MQW and two SL samples. MQW1 is doped in the barriers at a high concentration. MQW2 is doped in the quantum well at a low concentration. SL1 is doped in the CdS ''quantum wells'' and SL2 is not doped at all. Thickness and doping parameters of these samples are listed in Table I.

The infrared absorption was measured using a Bruker Fourier transform spectrometer IFS 113v. The samples were placed in a liquid-He-flow cryostat. Transmission spectra

 

TABLE I. Sample parameters of the investigated MQW and SL samples.

| Parameter | MQW1 | MQW2 | SL1 | SL2 |
|---|---|---|---|---|
| Number of periods | 20 | 20 | 140 | 140 |
| CdS width (nm) | 2.7 | 2.2 | 2.0 | 3.0 |
| ZnSe width (nm) | 30 | 30 | 2.0 | 1.9 |
| Donor density CdS ($cm^{-3}$) | - | $3\times10^{17}$ | $8\times10^{18}$ | - |
| Donor density ZnSe ($cm^{-3}$) | $12\times10^{18}$ | - | - | - |
| 2D electron density ($cm^{-2}$) | $1.3\times10^{13}$ | $6\times10^{10}$ | - | - |

were recorded in *p* polarization and *s* polarization mostly at 10 K or 295 K. In order to observe strong intersubband and interminiband absorption signals, the samples have been prepared in the so-called waveguide geometry by polishing two parallel facets at an angle of $39°\pm1°$ to the surface plane. Because the midinfrared refractive index of GaAs ($n_{GaAs}\approx3.3$) differs from that of the II-VI materials ($n_{CdS}\approx2.3$, $n_{ZnSe}\approx2.3$), the infrared beam is refracted at the GaAs-ZnSe interface and propagates at more ''flat'' angles through the heterostructure, thus enhancing the electric field component along the confinement direction (see inset of Fig. 2). The beam is totally reflected at the GaAs-ZnSe interface at angles above 44°. The facet angle of 39° has been chosen in order to avoid this total reflection.

Deliberate variation of the ground-state population is obtained by photoexcitation of electrons from the ZnSe valence band to the first CdS conduction subband or miniband. This interband transition is pumped using the 488-nm line of an argon ion laser. As the laser energy of 2.54 eV is smaller than the ZnSe band gap, the photoexcitation is resonant into the confined states of the quantum wells and superlattices.

## III. CALCULATION OF TRANSITION ENERGIES

The heterostructure energy levels were calculated in the single-particle envelope-function approximation considering nonparabolic bands, and many-particle effects were treated as later on corrections.

### A. Band nonparabolicity

The subband levels were obtained from the standard transcendental equation for a rectangular potential in the parabolic limit.[13] Nonparabolicity was considered through energy-dependent masses in this equation,[13,14] given by $m(E)=\hbar^2k^2/[2E(k)]$. The electron energy dispersions $E(k)$ were described by the three-band Kane model.[15] The input parameters of this model—the band-edge mass $m_{\Gamma_6}$, the band-gap energy $E_G$, and the spin-orbit splitting $\Delta_{SO}$-were taken as follows: $m_{\Gamma_6}=0.19m_0$ (see below), $E_G=2.5$ eV, and $\Delta_{SO}=0.07$ eV for CdS and $m_{\Gamma_6}=0.16m_0$, $E_G=2.82$ eV, and $\Delta_{SO}=0.43$ eV for ZnSe; $m_0$ denotes the free-electron mass. The CdS conduction band dispersion of the Kane model was compared to recent HPT and linear combination of atomic orbitals (LCAO) results of Refs. 16 and 17, respectively, and found to lay in between of these two numerical curves. It is considered to be reliable up to 800 meV electron energy. The energy-dependent mass was calculated numerically from the three-band model. It was found that the simple formula[18–20]

$$m(E)=m_{\Gamma_6}\left[1+\left(1-\frac{m_{\Gamma_6}}{m_0}\right)^2\frac{E}{E_G}\right] \tag{3.1}$$

provides a good approximation, even in the evanescent-state regime. The deviation from the three-band model amounts to less than 2% at 800 meV electron energy. Note that the spin-orbit splitting in CdS is very small (70 meV); hence, it can be ignored. The CdS/ZnSe single-particle energies were calculated using Eq. (3.1) with parameters given above. Remaining adjustable parameters were the well width and the band offset. A level shift caused by band bending in the quantum well is not considered, since the theory is applied to well-doped samples only with uniform doping. The effect of nonparabolicity on the intersubband transition energy is illustrated in Fig. 1, discussed in the next section.

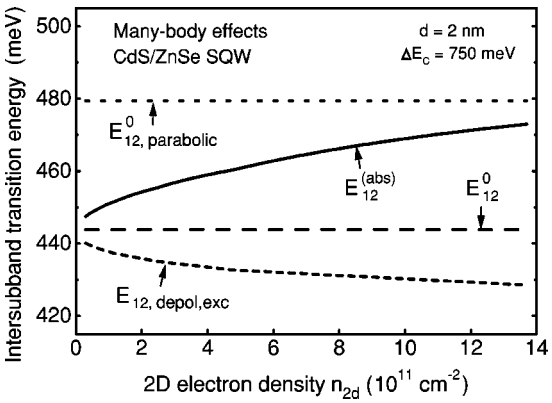


FIG. 1. Calculated $E_{12}$ intersubband transition energy as function of the 2D free-electron density for a CdS/ZnSe single quantum well (well width 2 nm and conduction band offset 750 meV). The straight lines represent the single-particle transition energy without (upper line) and with nonparabolicity (lower line). The short-dashed curve includes depolarization and excitonlike effects. The solid curve in addition includes the exchange and direct Coulomb interaction.

### B. Many-body effects

Two many-body phenomena are considered, the exchange interaction and the direct Coulomb interaction in a doped quantum well.[21] The shifts caused by the exchange interaction on the level positions of the first subband, $E^{(1)}$, and of the second subband, $E^{(2)}$, were calculated using the following expressions derived in Ref. 22:

$$E^{(1)}_{exch}(k)=-\frac{e^2k_F}{4\pi\epsilon\epsilon_0}\left[\frac{2}{\pi}\hat{E}\left(\frac{k}{k_F}\right)-\left(\frac{1}{6}-\frac{5}{8\pi^2}\right)k_FL\right]$$

for $k<k_F$ and

$$E_{exch}^{(1)}(k) = -\frac{e^2 k_F}{4\pi\epsilon\epsilon_0}\left[\frac{2}{\pi}\left\{\frac{k}{k_F}\hat{E}\left(\frac{k_F}{k}\right) + \frac{k_F^2 - k^2}{kk_F}\hat{K}\left(\frac{k_F}{k}\right)\right\} - \left(\frac{1}{6} - \frac{5}{8\pi^2}\right)k_F L\right]$$

for $k > k_F$ for the first subband and for the second subband

$$E_{exch}^{(2)}(k) = -\frac{5e^2 k_F^2 L}{36\pi^3\epsilon\epsilon_0}.$$

Here $k_F = \sqrt{2\pi n_{2d}}$ is the Fermi wave vector with $n_{2d}$ the two-dimensional electron density. $\hat{E}$ and $\hat{K}$ are complete elliptic integrals, $k$ is the in-plane wave vector, and $L$ the well width.

The direct Coulomb interaction causes shifts approximately described by[21]

$$E_{direct}^{(1)} = \frac{3n_{2d}e^2 L}{8\pi^2\epsilon\epsilon_0}$$

and

$$E_{direct}^{(2)} = \frac{n_{2d}e^2 L}{4\pi^2\epsilon\epsilon_0}.$$

The transition energy $E_{12}$ becomes

$$E_{12} = E_{12}^0 + \Delta E_{exch} + \Delta E_{direct},$$

with $E_{12}^0$ the single-particle transition energy, $\Delta E_{exch} = E_{exch}^{(2)} - E_{exch}^{(1)} > 0$ and $\Delta E_{direct} = E_{direct}^{(2)} - E_{direct}^{(1)} < 0$. Since $|\Delta E_{exch}|$ is greater than $|\Delta E_{direct}|$, the transition energy shifts to the blue with increasing electron density.

The measured peak position of the absorption signal is shifted from the $E_{12}$ transition energy owing to the depolarization shift,[23,24] the excitonlike effect,[25] and the coupling to longitudinal optical phonons (plasmon phonon coupling). The effect of the phonon coupling is negligible, since the transition energies in discussion distinctly exceed the energies of the involved phonons. The depolarization shift and excitonlike effect were considered using the formalism of Ref. 24. There the absorption peak position $E_{12}^{(\mathrm{abs})}$ is given by

$$E_{12}^{(\mathrm{abs})} = E_{12}\sqrt{1 + \alpha_{12} - \beta_{12}},$$

with the depolarization shift

$$\alpha_{12} = \frac{2e^2 n_{2d}}{\epsilon_b\epsilon_0 E_{12}}\int_{-\infty}^{+\infty} dz\left(\int_{-\infty}^{z}\phi_1(z')\phi_2(z')dz'\right)^2$$

and excitonlike effect

$$\beta_{12} = -\frac{2n_{2d}}{E_{12}}\int_{-\infty}^{+\infty} dz\ \phi_1(z)^2\phi_2(z)^2\frac{\partial V_{xc}(n_{3d}(z))}{\partial(n_{3d}(z))}.$$

$\epsilon_b$ is the background dielectric constant, and $V_{xc}(n_{3d}(z))$ is the exchange correlation potential[25] as a function of the local sheet density $n_{3d}(z) = n_{2d}|\phi_1(z)|^2$. Here $\phi_1(z)$ and $\phi_2(z)$ are the confined wave functions of the first and second subbands, respectively.

The effect of these shifts as function of the sheet electron density is illustrated in Fig. 1. The curves were calculated for a CdS/ZnSe single quantum well with a well width of 2 nm and a conduction band offset of 750 meV (see below). The two straight lines denote the single-particle transition energies without many-body effects. The upper one, labeled by $E_{12,parabolic}^0$, corresponds to the parabolic limit and is shown for comparison purposes only. The lower one, labeled by $E_{12}^0$, is the single-particle transition energy including the conduction band nonparabolicity. Inclusion of nonparabolicity results in a redshift of 8% (38 meV), and hence makes an important effect at a 2-nm well width. The two curved lines illustrate the inclusion of many-body effects to the transition energy $E_{12}^0$. The lower curve (short dashed line), labeled by $E_{12,depol,exc}$, corresponds to the inclusion of the depolarization shift $\alpha_{12}$ and the excitonlike effect $\beta_{12}$ only, as given by $E_{12,depol,exc} = E_{12}^0(1 + \alpha_{12} - \beta_{12})^{1/2}$. Inclusion of these two effects causes a net redshift with increasing electron density. This means that the excitonlike effect dominates the depolarization shift in CdS/ZnSe heterostructures, in contrast to GaAs-based heterostructures, where the opposite applies and the two effects cause a net blueshift.[22] The upper curve (solid line), labeled by $E_{12}^{(abs)}$, includes, additionally to the depolarization shift and the excitonlike effect, the exchange interaction and the direct Coulomb interaction. Inclusion of these interactions outweighs the redshift of the depolarization and excitonlike effect and results in an overall blueshift of the absorption peak energy.

## IV. CdS/ZnSe MULTIPLE QUANTUM WELLS

### A. $E_{12}$ intersubband transition

Figure 2 shows the transmission spectrum in *p* polarization, $T_P$, divided by that in *s* polarization, $T_S$, of the barrier-doped sample MQW1 ($n_{2D} = 1.3\times10^{13}$ cm$^{-2}$). The ordinate is the negative logarithm of this ratio corresponding to the absorption. The lower inset shows the waveguide geometry and the light path of the infrared beam with an indication of the electric field directions of the *s* and *p* polarization. The infrared beam typically undergoes one or two internal reflections in the sample. The midinfrared absorption signal observed between 2500 and 4000 cm$^{-1}$ is assigned to the excitation of electrons from the first subband to the second subband. The absorption reaches a value of 0.23 at the peak energy of 404 meV. This remarkable value results from the high ground-state electron density and the small in-plane inclination of the infrared beam of only 28° because of the refractive index step at the III-V/II-VI interface.[26] The relatively large width of 38 meV reflects the low mobility observed in electrically contacted two-dimensional electron gas (2DEG) structures.[10] The oscillator strengths extracted from the integrated absorption of a number of different samples are found to agree reasonably with theory.[27]

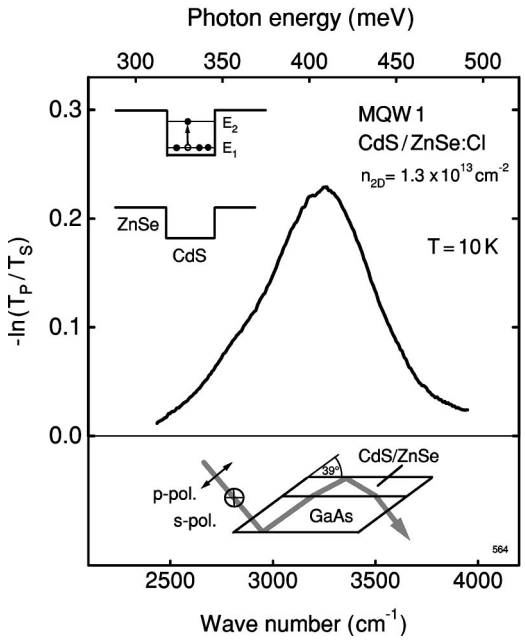


FIG. 2. Intersubband absorption spectrum of the heavily doped MQW1.

### B. Selection rules

Since the spin-orbit splitting is very small in CdS, the polarization selection rule for intersubband transitions is expected to be fulfilled;[28] that is, the transition matrix element should be nonzero only for electric field components along the confinement direction ($p$ polarization). However, strain and interface effects in the highly strained, thin quantum well samples may affect the validity of the polarization selection rule. In order to test it, polarization-dependent measurements were performed. Figure 3(a) shows a set of $-\ln(T_\gamma/T_s)$ curves of sample MQW1 measured at different polarization angles $\gamma$. Here $\gamma=0°$ corresponds to $p$ polarization (maximum coupling) and $\gamma=90°$ to $s$ polarization (no coupling).

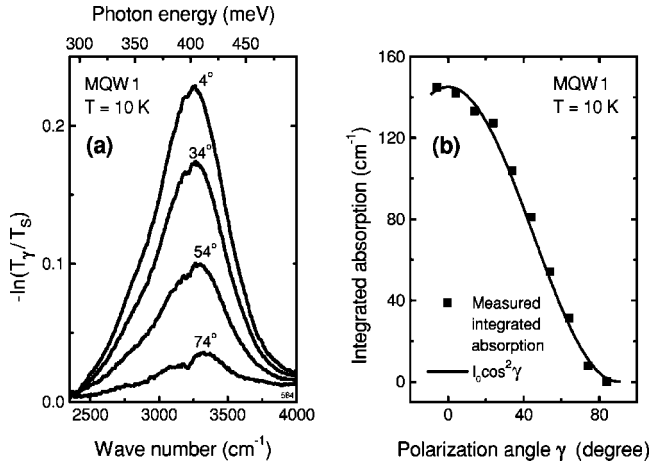


FIG. 3. (a) Intersubband absorption spectra of MQW1 measured at four different polarization angles $\gamma$. (b) Integrated intersubband absorption against the polarization angle (symbols) and a fit to $\cos\gamma^2$ (solid line).

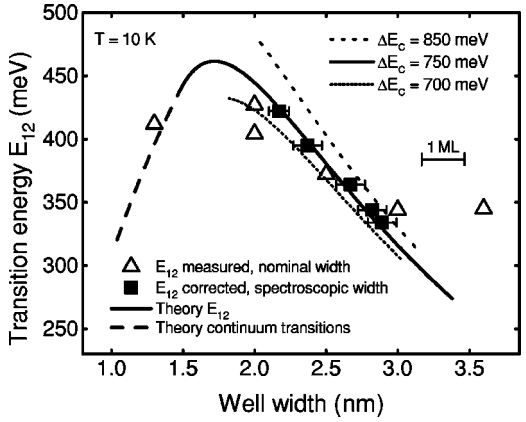


FIG. 4. Measured intersubband transition energies against well width before (open triangles) and after (solid squares) individual well width and many-body corrections. Lines represent the single-particle transition energy for bound-to-bound and bound-to-continuum transitions with conduction band offsets as indicated.

Figure 3(b) shows the measured integrated absorption (solid squares) against the polarization angle. From simple geometric optics, the angular dependence of the integrated intersubband absorption is predicted to vary as $\cos^2\gamma$. This prediction is shown by the solid curve in Fig. 3(b). It is in excellent agreement with the experimental data. As a result, the polarization selection rule is well fulfilled for the conduction band intersubband transitions in CdS/ZnSe quantum wells, and substantial strain or interface effects do not show up in the present samples.

### C. Well width dependence and conduction band offset

Since the intersubband transition energies in the small quantum wells depend critically on well width, we did not rely on the nominal thicknesses only, but derived a well width by measuring the interband transition energy as well as the intersubband transition energy. The interband transition energies were obtained from photoluminescence spectra correcting for the Stokes shift along Ref. 29 and for the many-body effects. An example of an interband photoluminescence spectrum is shown in Fig. 7(a) below. Because the same model is used to calculate the intersubband as well as the interband transition energy, the two adjustable parameters of the model can both be treated as fit parameters. Fitting the model to the two observed transition energies thus provides the well width and the band offset of a given sample. Five well-doped MQW samples have been analyzed in this way. The well widths determined by the spectroscopic method agreed satisfactorily to the nominal widths ($\pm1$ monolayer) with a single exception where it was smaller by 20%. The conduction band offsets scattered around 750 meV within a 50 meV range.

Figure 4 shows the intersubband transition energies $E_{12}$ of these five samples against the well width. Open triangles denote the measured absorption peak energies plotted against the *nominal* width. Solid squares denote the single-particle transition energies: that is, after correction by many-body effects, plotted against the *spectroscopic* width. Because the

samples are doped differently, the many-body corrections had to be made individually and could not be included in a theoretical curve. The solid curve represents the calculated single-particle transition energy using a conduction band offset of 750 meV. A good agreement is observed between the theoretical and the experimental transition energies, provided the *spectroscopic* well widths are used and many-body corrections are taken into account. The many-body corrections are smaller compared to the well width corrections, but they are significant and improve the agreement. One conclusion is that the quantum wells are sufficiently well described by a rectangular model potential. Second, the determination of the well width from intersubband and interband transitions appears to be consistent and to give the ''true'' widths within the model approximations. A third conclusion concerns the energy range of intersubband transitions in CdS/ZnSe MQW's obtainable by varying the well width. The solid curve indicates that the transition energy is tunable between 150 meV and 450 meV by varying the well width between 4.5 nm and 1.7 nm.

The offset value of the strained quantum well obtained by fitting is $750^{+100}_{-50}$ meV. The error limits correspond to the dotted lines in Fig. 4. At larger well widths, the fit becomes less sensitive to the offset value, the latter being fixed mainly by the small width samples. The obtained value is 70 meV smaller than that determined recently from a series of single quantum wells[8] (in this reference, an exciton binding energy of 20 meV was erroneously taken into account, so the offset of the strained quantum well would be actually 820 meV). The smaller offset value in the present samples is attributed to an increased amount of intermixing due to the higher substrate temperature compared to that used for preparation of the previous samples (140 °C higher). If the previous samples are assumed to have binary CdS quantum wells, the 70-meV offset reduction would correspond to about 12% zinc admixture into the quantum well.

### D. Temperature dependence

The temperature dependence of the intersubband transition energy has been measured on the lightly well-doped sample MQW2 ($n_{2D}=6\times10^{10}$ cm$^{-2}$) because of its sharper absorption line. The transition energy decreases by nearly 3 meV between 10 K and 295 K as shown in Fig. 5. This decrease translates to a decrease of the conduction band offset of 8 meV, assuming the many-body correction of 5 meV and all other parameters to be temperature-independent. About 1 meV may be attributed to the strain-induced lowering of the CdS conduction band edge by thermal misfit to the ZnSe. The remaining 7 meV are attributed to differences in the band gap shrinkage between the CdS and the ZnSe. This is a small change of only 1%; that is, the conduction band offset does not depend very much on temperature.

### E. Photoinduced intersubband absorption

Figure 6(a) shows the intersubband absorption spectrum of MQW2 measured at 10 K. The absorption curve fits to a

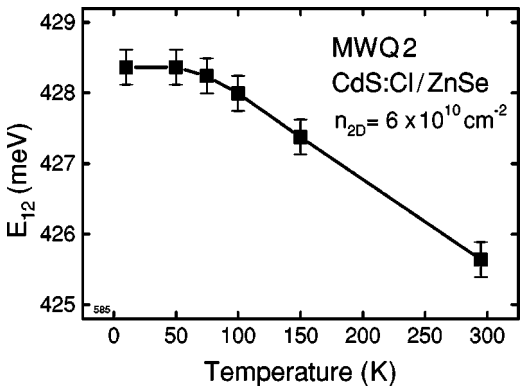


FIG. 5. Measured temperature dependence of the intersubband absorption peak energy of MQW2 (the line is a guide for the eye only).

Lorentzian line shape with a full width of half maximum of 16.7 meV. The strength of the observed infrared absorption suggests an occupation number of the subband ground state of the order of a few $10^{10}$ cm$^{-2}$, in agreement with the nominal value of $6\times10^{10}$ cm$^{-2}$. Figure 6(b) shows the spectrum of the photoinduced intersubband absorption (PIA), $-\ln(T_{p*}/T_p)$. Here $T_{p*}$ denotes the *p*-polarized transmission spectrum under interband laser excitation, $T_p$, as usual, without laser excitation. The PIA spectrum has a line shape similar to that of the absorption spectrum of Fig. 6(a) due to doping and has its maximum at the same energetic position. Therefore, the photoexcitation of additional electrons into the first subband does not change the spectral distribution of the 2DEG in the first subband.

In order to discuss the dependence on excitation density, first the population density as function of the laser intensity

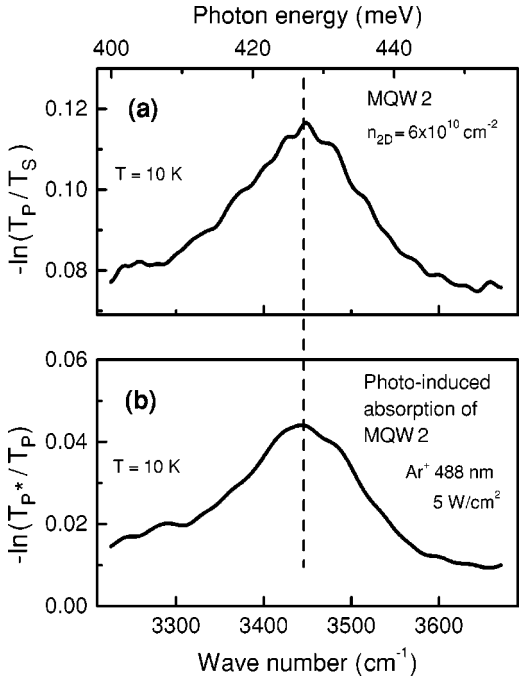


FIG. 6. (a) Measured intersubband absorption spectrum of MQW2. (b) Photoinduced intersubband absorption of MQW2.

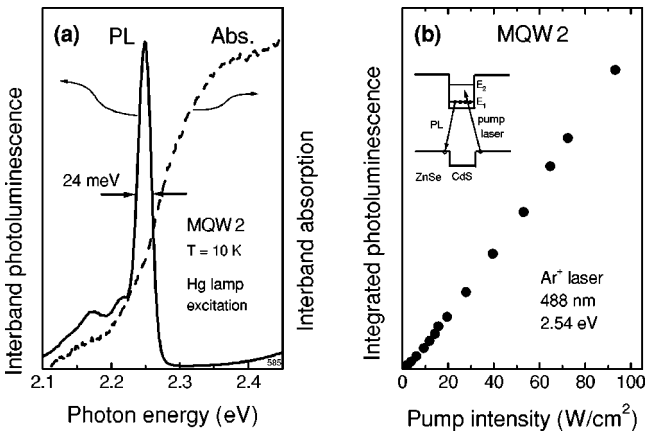


FIG. 7. (a) Photoluminescence and absorption spectra of MQW2 in the energy range of the lowest interband transition. (b) Integrated interband photoluminescence of MQW2 as function of the laser power.

is studied from the interband photoluminescence. The interband photoluminescence and the interband absorption spectrum of MQW2 are shown in Fig. 7(a). No excitonic features are observed in the absorption spectrum as a result of the type-II band alignment, in agreement with the absence of a spectral shift of the PIA spectrum. Figure 7(b) shows the integrated interband photoluminescence against the exciting laser intensity. The dependence on laser intensity is linear up to 100 $\mathrm{W\,cm^{-2}}$, meaning that the total density of photoexcited electron-hole pairs varies linear in the considered density regime. On the other hand, the integrated photoinduced intersubband absorption (IPIA) grows very rapidly with low laser intensities ($\leqslant 1$ $\mathrm{W\,cm^{-2}}$) and saturates at excitation intensities above 1 $\mathrm{W\,cm^{-2}}$, i.e., at photoinduced carrier densities of about $5\times10^{10}$ $\mathrm{cm^2}$ (Fig. 8). The fast increase of the IPIA at low laser intensities suggests a lifetime in the order of 1 $\mu$s. Therefore, it can be concluded that the PIA is due to a subgroup of long-lived photoexcited electrons. Since the photogenerated electrons are not distinguishable from the already existing ones, the long lifetime must be due to a subgroup of photoexcited holes.

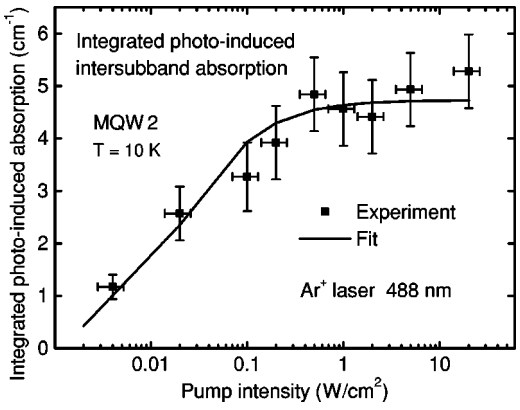


FIG. 8. Integrated photoinduced intersubband absorption of MQW2 as function of the laser power. The fit corresponds to Eq. (4.1).

Two possible quantitative scenarios which can describe this behavior are the following: (i) Most of the photogenerated holes are localized near the CdS/ZnSe interface due to Coulomb interactions until they recombine radiatively or nonradiatively with an electron of the two-dimensional electron gas. The almost linear dependence of the photoluminescence signal on the laser intensity is determined by these dominating recombination processes. The small part of the photoexcited holes which are localized in the ZnSe barriers away from the interface have a longer lifetime due to the smaller overlap of the wave functions and a reduced recombination probability. In contrast to the interband photoluminescence the photoinduced intersubband absorption is very sensitive to this subgroup of long-lived holes. Then the saturation of the PIA signal is a consequence of the limited number of hole localization centers. (ii) The behavior of the interband photoluminescence is explained in the same way as above. A small part of the photoexcited holes can also recombine with electrons of the conduction band of the ZnSe barriers leading to an effective longer lifetime of the photogenerated electrons. In this case the saturation can be explained by the limited number of electrons in the conduction band of the nonintentionally doped ZnSe barrier.

According to Ref. 30, the experimentally determined values for the IPIA have been fitted by

$$\mathrm{IPIA}=kN_{\mathrm{PIA}}=k\frac{g\tau N_s}{g\tau+N_s}, \tag{4.1}$$

where $k$ is a constant, $g$ is the photoexcitation generation rate, and $N_s$ is the saturation density. The parameters obtained from the fit shown in Fig. 8 are $N_s=5\times10^{10}$ $\mathrm{cm^{-2}}$ and $\tau=6$ $\mu$s.

## V. CdS/ZnSe SUPERLATTICES

### A. Interminiband transitions in the conduction band

The selection rules for transitions between the first $E_1(k_\parallel)$ and the second miniband $E_2(k_\parallel)$ in the conduction band are the same as in case of the intersubband transitions. However, the width of the infrared absorption peaks of interminiband transitions is not determined by collisional or homogeneous broadening, but rather by the intrinsic width of the involved minibands. This increased width of the interminiband absorption spectra is visible in all spectra shown in Fig. 9.

Figure 9(a) shows the calculated miniband dispersion using a conduction band offset of 750 meV and parameters corresponding to that of the superlattice sample SL1. It has been determined by solving the standard transcendental equation[13] using energy-dependent effective masses to take account of the nonparabolicity. The calculated width of the first miniband is 26 meV. The calculated interminiband transition energy between the first and second minibands is 378 meV at the edge of the Brillouin zone. Transition energies above about 420 meV belong to transitions into continuum states.

Figure 9(b) shows the interminiband absorption spectra measured at three different temperatures on SL1, which has uniformly doped CdS layers. Using the tight-binding model,

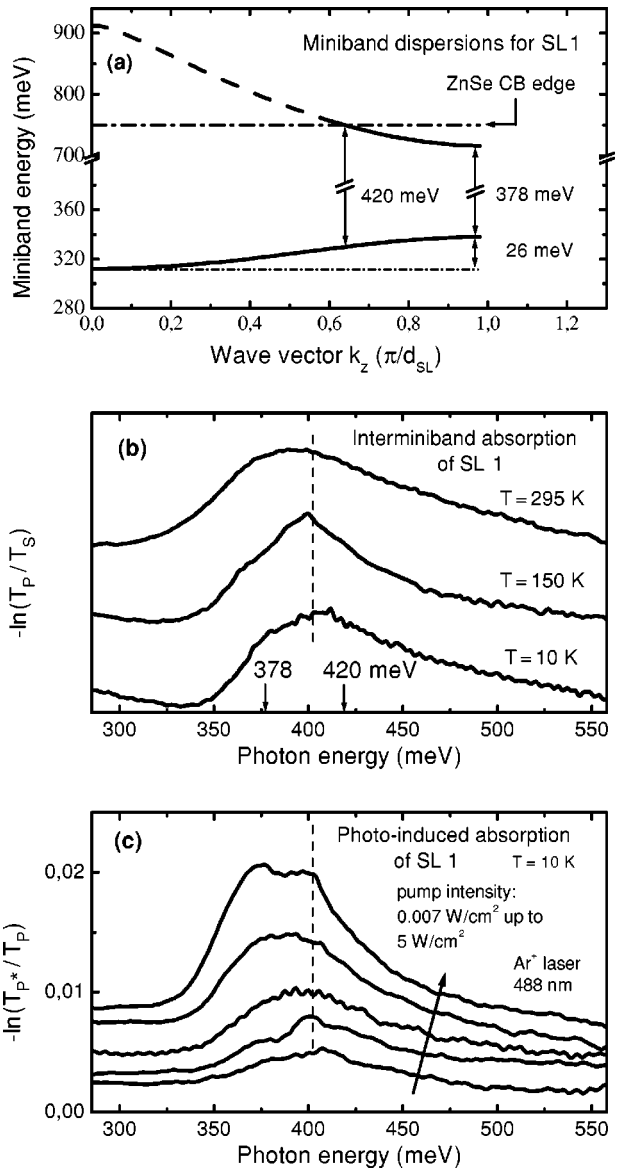


FIG. 9. (a) Calculated miniband dispersions of SL1 with a period of $d_{SL}=4$ nm, (b) interminiband absorption spectra of SL1 as function of temperature (for clarity the spectra are shifted vertically), and (c) photoinduced interminiband absorption spectra of SL1 recorded at various laser intensities. The dashed vertical line marks the peak maximum at low temperature and low excitation density.

the Fermi level is estimated to be at most 25 meV above the minimum of the lowest miniband, meaning that only the first miniband is occupied. Therefore and because of the agreement with the calculated transition energies, the observed maximum in the midinfrared absorption spectra is attributed to electronic transitions from the first to the second miniband. In analogy to investigations on III-V semiconductor superlattices,[31] asymmetric absorption bands are observed which are explained by the dispersion of the minibands. With increasing temperature, the interminiband absorption maxima in Fig. 9(b) are observed to shift red. This redshift is attributed to some redistribution of the population in the first miniband: with increasing temperature, states at increasingly

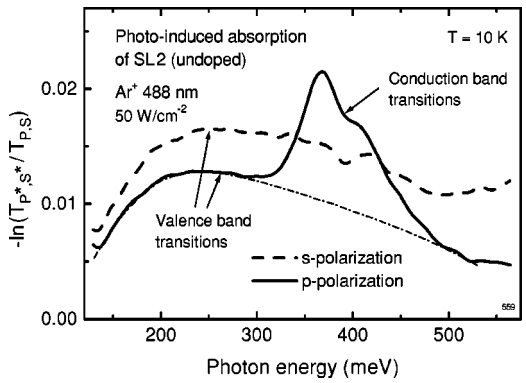


FIG. 10. Photoinduced interminiband absorption of SL2 for *s* and *p* polarization.

higher wave vectors become occupied. Lifting an electron from these states into the continuum or into the second miniband then requires less energy, increasing absorption on the low-energy side.

The measured photoinduced interminiband absorption spectra of SL1 are shown in Fig. 9(c). With increasing pump intensity tuned from zero up to 5 $W\,cm^{-2}$, the absorption becomes stronger. This effect can be understood by an increased population of the lowest miniband due to photoexcited electrons. Because of the greater number of periods of the superlattice compared to the MQW, the absorption of the pump laser beam is more efficient, generating a larger electron density. The photoinduced interminiband absorption is observed to shift red with increasing pump intensity. This redshift is interpreted by a filling of the first miniband to higher wave vectors. At the highest pump intensity, the spectrum indicates the presence of two ''peaks,'' possibly reflecting the increased density of states at the center and the edge of the Brillouin zone. Similarly to the change of occupation by a temperature increase, the filling of the first miniband decreases the transition energy of the interminiband transition. It has already been shown that the miniband dispersion can be evaluated from the temperature dependence of the interminiband absorption profile.[31] We suggest here that the dispersion may also be evaluated by studying the *photoinduced* interminiband absorption in dependence on the photoexcitation density.

### B. Interminiband transitions in the valence band

In contrast to electronic transitions in the conduction band discussed so far, transitions between minibands built up from different valence bands, like heavy hole (HH), light hole (LH), and spin-orbit split-off (SO) bands, are allowed only for light polarized perpendicular to the confinement direction.[32,33] Experimentally, intersubband valence band transitions have already been observed in *p*-type-doped Si/SiGe heterostructures. Figure 10 shows the photoinduced interminiband absorption spectra of the undoped sample SL2, recorded for *s*- and *p*-polarized infrared beams. In *s* polarization, a broad asymmetric band is observed between 150 meV and 500 meV. It is assigned to photoinduced interminiband transitions between the miniband ground states

built up from HH-, LH-, and SO- valence bands. In *p* polarization, the same band is observed, superimposed by a more sharp absorption feature around 400 meV. This feature is assigned to interminiband transitions in the conduction band. The appearance of the valence band transitions in *p* polarization is related to the fact the infrared beam is inclined to the layer plane and in *p* polarization has also an electric field component perpendicular to the confinement direction. The assignment of the broad absorption band to transitions in the valence bands is supported by a calculation. The calculated transition energies for HH1→SO1 and LH1→SO1 are situated at about 360 meV and 260 meV, respectively. We note that, while intersubband transitions in the valence bands of *p*-type heterostructures are well known, valence band interminiband transitions of superlattices have not yet been reported.

## VI. ELECTRON MASS OF CUBIC CdS

The effective electron mass of cubic CdS has been determined recently in Ref. 8 from a fit of the interband transition energies of CdS/ZnSe single quantum wells with a value of $(0.18\pm0.5)m_0$. In principle, the mass should be determined more precisely from infrared reflection spectroscopy and known carrier densities from bulk samples. A series of degenerately doped thick layers ($>1$ $\mu$m) of cubic CdS was prepared and investigated by Hall effect measurements.[9] These data yield the free-electron densities $n_{3d}$. The screened plasma frequencies $\omega_p$ of these samples were obtained from infrared reflection spectra recorded at nearly normal incidence to the surface and evaluated by a Drude-Lorentz fit. As an example, Fig. 11(a) shows the reflection spectrum of a CdS layer with $n_{3d}=7.4\times10^{19}$ cm$^{-3}$ in the frequency range of the plasmon resonance. The minimum at 4200 cm$^{-1}$ is caused by Fabry-Perot interferences and is used to determine sample thickness additionally. The dashed curve is the Drude-Lorentz fit and reproduces well the measured spectrum except a small dip at around 3200 cm$^{-1}$ the origin of which is unknown.

The screened plasma frequency is given by[34]

$$\omega_p=\sqrt{\frac{n_{3d}e^2}{\epsilon_b\epsilon_0 m_{\mathrm{op}}}}, \tag{6.1}$$

where $m_{\mathrm{op}}$ is the optical effective mass. The optical effective mass relates the Fermi velocity to the Fermi wave vector and is given by (spherical Fermi surface)

$$\frac{1}{m_{\mathrm{op}}}=\frac{1}{\hbar^2 k_{\mathrm{F}}}\left[\frac{dE(k)}{dk}\right]_{k_{\mathrm{F}}}. \tag{6.2}$$

A nonparabolic band $E(k)$ means a dependence of the optical effective mass on the free-carrier density. This dependence can be approximately described, after neglect of the small spin-orbit splitting, by[35]

$$\frac{1}{m_{op}}=\frac{1}{m_{\Gamma_6}}\left[1-\left(1-\frac{m_{\Gamma_6}}{m_0}\right)^2\frac{\hbar^2(3\pi^2 n_{3d})^{2/3}}{m_{\Gamma_6}E_G}\right]. \tag{6.3}$$

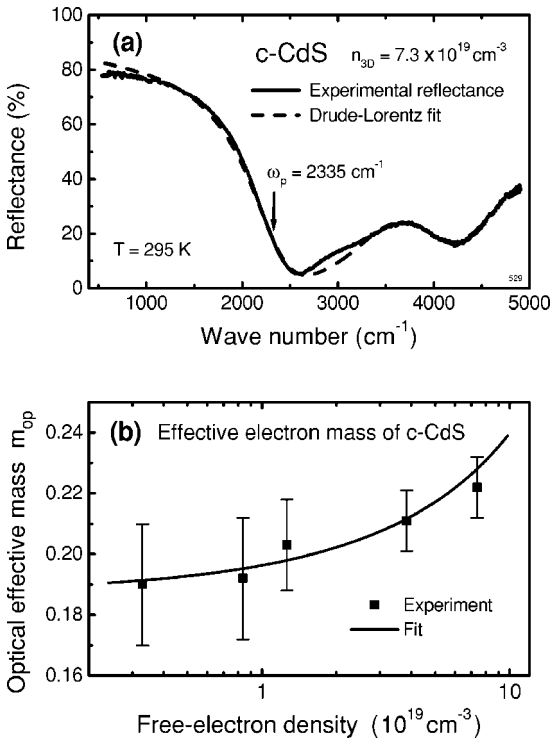


FIG. 11. (a) Measured and calculated reflection spectra of a heavily *n*-type-doped *c*-CdS layer. (b) The optical effective electron mass as function of the free-electron density. The line is a fit of Eq. (6.3).

Figure 11(b) shows experimental optical masses of five samples doped between $3\times10^{18}$ cm$^{-3}$ and $8\times10^{19}$ cm$^{-3}$. They were determined through Eq. (6.1) from the measured free-electron densities $n_{3d}$ and plasma frequencies $\omega_p$. The solid curve is a fit of Eq. (6.3) with the band edge mass $m_{\Gamma_6}$ as fit parameter. The resulting electron mass is $m_{\Gamma_6}=(0.19\pm0.01)m_0$. This value is within the range of electron masses reported for hexagonal CdS (Ref. 36) and is more precise by a factor of 5 compared to the above-mentioned result from CdS quantum wells.

## VII. CONCLUSIONS

Strong intersubband and interminiband absorption signals have been observed in *n*-type-doped CdS/ZnSe quantum well and superlattice samples prepared in a waveguide geometry. This is a consequence of the high doping levels attainable in this materials and an efficient coupling of the infrared beam caused by the refractive index step at the II-VI/GaAs substrate interface. Polarization-dependent measurements verified the polarization selection rule for conduction band transitions. Experimentally observed transition energies are in good agreement with those calculated, if many-body effects and conduction band nonparabolicity are taken into account, and if corrected well widths are used. The actual well widths were determined by fitting the measured intersubband and interband transition energies. The conduction band offset of the strained quantum well is derived to be $750^{+100}_{-50}$ meV for the present samples. On this basis it is predicted that, by

varying the well width, the intersubband absorption can be tuned between 150 meV and 450 meV. This might be interesting for an application as midinfrared detector.

Photoinduced intersubband and interminiband absorption is studied as function of the photoexcitation density. In contrast to the linear behavior of the interband photoluminescence intensity, the intersubband absorption of quantum wells shows a nonlinear saturation behavior which has been explained by recombination and localization processes. In superlattices, evidence for valence band interminiband transitions was observed. It has been demonstrated that the pump-probe spectroscopy is a very sensitive means to study the electron distribution in the lowest miniband or to learn about the properties of excited electron hole pairs in a two-dimensional electron gas.

Finally, the effective electron band-edge mass of cubic CdS has been determined to $m_{\Gamma_6}=(0.19\pm0.01)m_0$ using a combination of Hall effect and infrared reflection measurements.

## ACKNOWLEDGMENT

This work was supported by the Deutsche Forschungsgemeinschaft.

*Also at Institut für Nanotechnologie, Universität Karlsruhe, Karlsruhe, Germany.

[1] G. Abstreiter and K. Ploog, Phys. Rev. Lett. **42**, 1308 (1979).

[2] L. C. West and S. J. Eglash, Appl. Phys. Lett. **46**, 1156 (1985).

[3] Qin-Sheng Zhu, X. B. Wang, Z. T. Zhong, X. C. Zhou, Y. P. He, Z. P. Cao, G. Z. Zhang, J. Xiao, X. H. Sun, H. Z. Yang, and Q. G. Du, Phys. Rev. B **57**, 12 388 (1998).

[4] T. Fromherz, E. Koppensteiner, M. Helm, G. Bauer, J. F. Nützel, and G. Abstreiter, Phys. Rev. B **50**, 15 073 (1994).

[5] R. L. Whitney, F. W. Adams, and K. F. Cuff, in *Intersubband Transitions in Quantum Wells*, in Vol. 288 of *NATO Advanced Study Institute, Series B: Physics*, edited by E. Rosencher, B. Vinter, and B. Levine (Plenum, New York, 1992).

[6] J. Faist, F. Capasso, C. Sirtori, D. L. Sivco, A. L. Hutchinson, M. S. Hybertsen, and A. Y. Cho, Phys. Rev. Lett. **76**, 411 (1996).

[7] R. Sizmann, P. Helgesen, H. Steen, T. Skauli, T. Colin, K. Gjonnes, and S. Lovold, Semicond. Sci. Technol. **8**, S296 (1993); A. M. de Paula, C. R. M. Oliviera, G. E. Marques, A. M. Cohen, R. D. Feldmann, R. F. Austin, M. N. Islam, and C. L. Cesar, Phys. Rev. B **59**, 10 158 (1999).

[8] A. Dinger, S. Petillon, M. Hetterich, M. Grün, and C. Klingshirn, Semicond. Sci. Technol. **14**, 595 (1999).

[9] M. Grün, A. Storzum, M. Hetterich, A. Kamilli, W. Send, and C. Klingshirn, J. Cryst. Growth **201/202**, 457 (1999).

[10] V. Kazukauskas, M. Grün, S. Petillon, A. Storzum, and C. Klingshirn, Appl. Phys. Lett. **74**, 395 (1999).

[11] B. K. Ridley, Phys. Rev. B **39**, 5282 (1989).

[12] S. Petillon, A. Dinger, M. Grün, M. Hetterich, C. Klingshirn, J. Liang, B. Weise, V. Wagner, and J. Geurts, J. Cryst. Growth **201/202**, 453 (1999).

[13] G. Bastard, *Wave Mechanics Applied to Semiconductor Heterostructures* (Les Editions de Physique, Paris, 1988).

[14] M. G. Burt, J. Phys.: Condens. Matter **4**, 6651 (1992).

[15] E. O. Kane, J. Phys. Chem. Solids **1**, 249 (1957).

[16] A.-B. Chen and A. Sher, *Semiconductor Alloys* (Plenum Press, New York, 1995).

[17] M.-Z. Huang and W. Y. Ching, J. Phys. Chem. Solids **8**, 977 (1985).

[18] D. C. Rogers, J. Singleton, R. J. Nicholas, C. T. Foxon, and K. Woodbridge, Phys. Rev. B **34**, 4002 (1986).

[19] U. Ekenberg, Phys. Rev. B **40**, 7714 (1989).

[20] P. Harrison and R. W. Kelsall, Physica E **2**, 468 (1998).

[21] K. M. S. V. Bandara, D. D. Coon, O. Byungsung, Y. F. Lin, and M. H. Francombe, Appl. Phys. Lett. **53**, 1931 (1988).

[22] M. O. Manasreh, F. Szmulowicz, T. Vaughan, K. R. Evans, C. E. Stutz, and D. W. Fischer, Phys. Rev. B **43**, 9996 (1991); M. O. Manasreh, F. Szmulowicz, T. Vaughan, K. R. Evans, C. E. Stutz, and D. W. Fischer, in Vol. 288 of *NATO Advanced Study Institute, Series B*: *Physics*, *Intersubband Transitions in Quantum Wells*, edited by E. Rosencher, B. Vinter, and B. Levine (Plenum, New York, 1992), p. 287.

[23] S. J. Allen, D. C. Tsui, and B. Vinter, Solid State Commun. **20**, 425 (1976).

[24] T. Ando, Solid State Commun. **21**, 133 (1977).

[25] W. L. Bloss, J. Appl. Phys. **66**, 3639 (1989).

[26] M. Göppert, R. Becker, S. Petillon, M. Grün, C. Maier, A. Dinger, and C. Klingshirn, J. Cryst. Growth **214/215**, 625 (2000).

[27] M. Göppert, R. Becker, S. Petillon, M. Grün, C. Maier, A. Dinger, and C. Klingshirn, Physica E **7**, 89 (2000).

[28] R. J. Warburton, C. Gauer, A. Wixforth, J. P. Kotthaus, B. Brar, and H. Kroemer, Phys. Rev. B **53**, 7903 (1996).

[29] M. Wilkinson, F. Yang, E. A. Austin, and K. P. O'Donnell, J. Phys.: Condens. Matter **4**, 8863 (1992).

[30] Y. Garini, E. Ehrenfreund, E. Cohen, Arza Ron, K. K. Law, J. L. Merz, and A. C. Gossard Phys. Rev. B **48**, 4456 (1993).

[31] M. Helm, W. Hilber, T. Fromherz, F. M. Peeters, K. Alavi, and R. N. Pathak, Phys. Rev. B **48**, 1601 (1993).

[32] Y. C. Chang and R. B. James, Phys. Rev. B **39**, 12 672 (1989).

[33] S. K. Chun, D. S. Pan, and K. L. Wang, Phys. Rev. B **47**, 15 638 (1993).

[34] F. Wooten, *Optical Properties of Solids* (Academic Press, New York, 1972).

[35] A. Raymond, J. L. Robert, and C. Bernard, J. Phys. C **12**, 2289 (1979).

[36] *Numerical Data and Functional Relationships in Science and Technology*, Landolt-Börnstein, New Series, Group III, Vol. 17b (Springer, Berlin, 1982).